

## RESEARCH ARTICLE

# Localization of all four ZnT zinc transporters in *Dictyostelium* and impact of ZntA and ZntB knockout on bacteria killing

Caroline Barisch<sup>‡</sup>, Vera Kalinina<sup>\*</sup>, Louise H. Lefrançois, Joddy Appiah, Ana T. López-Jiménez and Thierry Soldati

## ABSTRACT

Professional phagocytes have developed an extensive repertoire of autonomous immunity strategies to ensure killing of bacteria. Besides phagosome acidification and the generation of reactive oxygen species, deprivation of nutrients and the luminal accumulation of toxic metals are essential to kill ingested bacteria or inhibit the growth of intracellular pathogens. Here, we used the soil amoeba *Dictyostelium discoideum*, a professional phagocyte that digests bacteria for nutritional purposes, to decipher the role of zinc poisoning during phagocytosis of nonpathogenic bacteria and visualize the temporal and spatial dynamics of compartmentalized, free zinc using fluorescent probes. Immediately after particle uptake, zinc is delivered to phagosomes by fusion with 'zincosomes' of endosomal origin, and also by the action of one or more zinc transporters. We localized the four *Dictyostelium* ZnT transporters to endosomes, the contractile vacuole and the Golgi complex, and studied the impact of *znt* knockouts on zinc homeostasis. We show that zinc is delivered into the lumen of *Mycobacterium smegmatis*-containing vacuoles, and that *Escherichia coli* deficient in the zinc efflux P<sub>1B</sub>-type ATPase ZntA are killed faster than wild-type bacteria.

**KEY WORDS:** *Dictyostelium*, Zinc transporter, Zinc poisoning, Bacteria killing, Phagocytosis

## INTRODUCTION

Transition metals, such as iron (Fe), zinc (Zn), manganese (Mn), cobalt (Co) and copper (Cu), are essential for the survival of all living organisms (Weiss and Carver, 2018). These metals are incorporated into active sites of metalloenzymes, and organize secondary structures such as the Zn<sup>2+</sup> finger domains of many proteins, including transcription factors. They are therefore implicated in a wide range of crucial biological processes. However, excess of these metals is toxic for living organisms, partially because they compete for metal-binding sites in enzymes. In this context, recent studies have revealed transition metals as a 'double-edged sword' during infection of phagocytic cells. Upon phagocytosis, the innate immune phagocyte restricts intravacuolar bacterial growth either by depleting essential metal ions (e.g. Fe<sup>2+</sup> and Mn<sup>2+</sup>) or by accumulating others, such as Cu<sup>2+</sup> and Zn<sup>2+</sup>,

to intoxicating concentrations (Flannagan et al., 2015; Lopez and Skaar, 2018). On the pathogen side, bacteria have evolved several strategies to survive excess of metal ions, both in the environment (Ducret et al., 2016; Gonzalez et al., 2018) and in contact with phagocytes (Botella et al., 2011). For instance, metal efflux transporters, such as cation diffusion facilitators and P-type ATPases, remove excess ions from the bacterial cytoplasm (Chan et al., 2010; Kolaj-Robin et al., 2015).

Recently, Zn<sup>2+</sup> poisoning was shown to be among the killing strategies of macrophages (Botella et al., 2011). Inside macrophages, free Zn<sup>2+</sup> mainly localizes to late endosomes and lysosomes, and to a smaller extent to early endosomes (Botella et al., 2011). Zn<sup>2+</sup> presumably enters cytoplasmic organelles by fusion with Zn<sup>2+</sup>-containing endosomes, called zincosomes, or by the direct action of one or several Zn<sup>2+</sup> transporters located at the membrane of the organelle. For example, Zn<sup>2+</sup> has been observed to accumulate in phagolysosomes containing the nonpathogenic bacteria *Escherichia coli*, contributing to their killing. In addition, Zn<sup>2+</sup> transporters are upregulated in macrophages infected with *Mycobacterium tuberculosis* and, after a cytosolic burst, free Zn<sup>2+</sup> is delivered and accumulates into the *Mycobacterium*-containing vacuole (MCV) 24 h after infection (Botella et al., 2011; Pyle et al., 2017; Wagner et al., 2005). Interestingly, vice versa, the expression of the P<sub>1</sub>-type Zn<sup>2+</sup>-exporting ATPase CtpC of *M. tuberculosis*, the Zn<sup>2+</sup>-exporting P<sub>1B</sub>-type ATPase ZntA of *E. coli* and *Salmonella enterica* serovar typhimurium, and the Zn<sup>2+</sup> cation diffusion facilitator of *Streptococcus pyogenes* increases during infection of human macrophages and neutrophils (Botella et al., 2011; Kapetanovic et al., 2016; Ong et al., 2014).

However, the import mechanism and temporal dynamics of Zn<sup>2+</sup> inside phagosomes containing nonvirulent and virulent bacteria are still poorly understood. Two families of Zn<sup>2+</sup> transporters, ZnT (Zn<sup>2+</sup> transporter Slc30a) and ZIP (Zrt/Irt-like protein Slc39a), have been described in metazoans and in the amoeba *Dictyostelium discoideum* (hereafter referred to as *Dictyostelium*) (Dunn et al., 2018; Kambe et al., 2015). In metazoans, the ZnT family consists of nine proteins (i.e. ZNT1–8 and ZNT10) that decrease cytosolic Zn<sup>2+</sup> levels by exporting it to the extracellular space or sequestering it into the lumen of organelles. In contrast, the 14 members of the ZIP family (i.e. ZIP1–14) catalyse the transport of free Zn<sup>2+</sup> from the extracellular space and organelles into the cytosol (Kambe et al., 2015). In *Dictyostelium*, four putative ZnT proteins and seven ZIP transporters have been identified, but the directionality of transport has not yet been experimentally confirmed (Dunn et al., 2018; Sunaga et al., 2008).

In recent years, *Dictyostelium* has evolved as a powerful model system to study phagocytosis and host-pathogen interactions, including cell autonomous defences and bacterial killing (Bozzaro et al., 2008; Dunn et al., 2018). The core machinery of the phagocytic pathway is highly conserved between human phagocytes and *Dictyostelium*, which digests and kills

Department of Biochemistry, Faculty of Science, University of Geneva, 30 Quai Ernest-Ansermet, Science II, 1211 Geneva-4, Switzerland.

<sup>\*</sup>Present address: Institute of Cytology, Russian Academy of Sciences, Tikhoretsky Ave. 4, 194064 St. Petersburg, Russia.

<sup>‡</sup>Author for correspondence (Caroline.Barisch@unige.ch)

© C.B., 0000-0002-1493-9006; V.K., 0000-0003-2053-5101; L.H.L., 0000-0002-9544-8435; J.A., 0000-0002-5847-7691; A.T.L., 0000-0002-0289-738X; T.S., 0000-0002-2056-7931

Received 27 June 2018; Accepted 17 October 2018

nonpathogenic bacteria for nutrition. First, bacteria are recognized by receptors at the plasma membrane, leading to an actin-dependent deformation of the membrane and the closure of the phagocytic cup

(Neuhaus et al., 2002). A few minutes after uptake, lysosomes fuse with the phagosome, delivering the vacuolar  $H^+$ -ATPase (vATPase), which acidifies the phagosomal lumen (pH <4) and

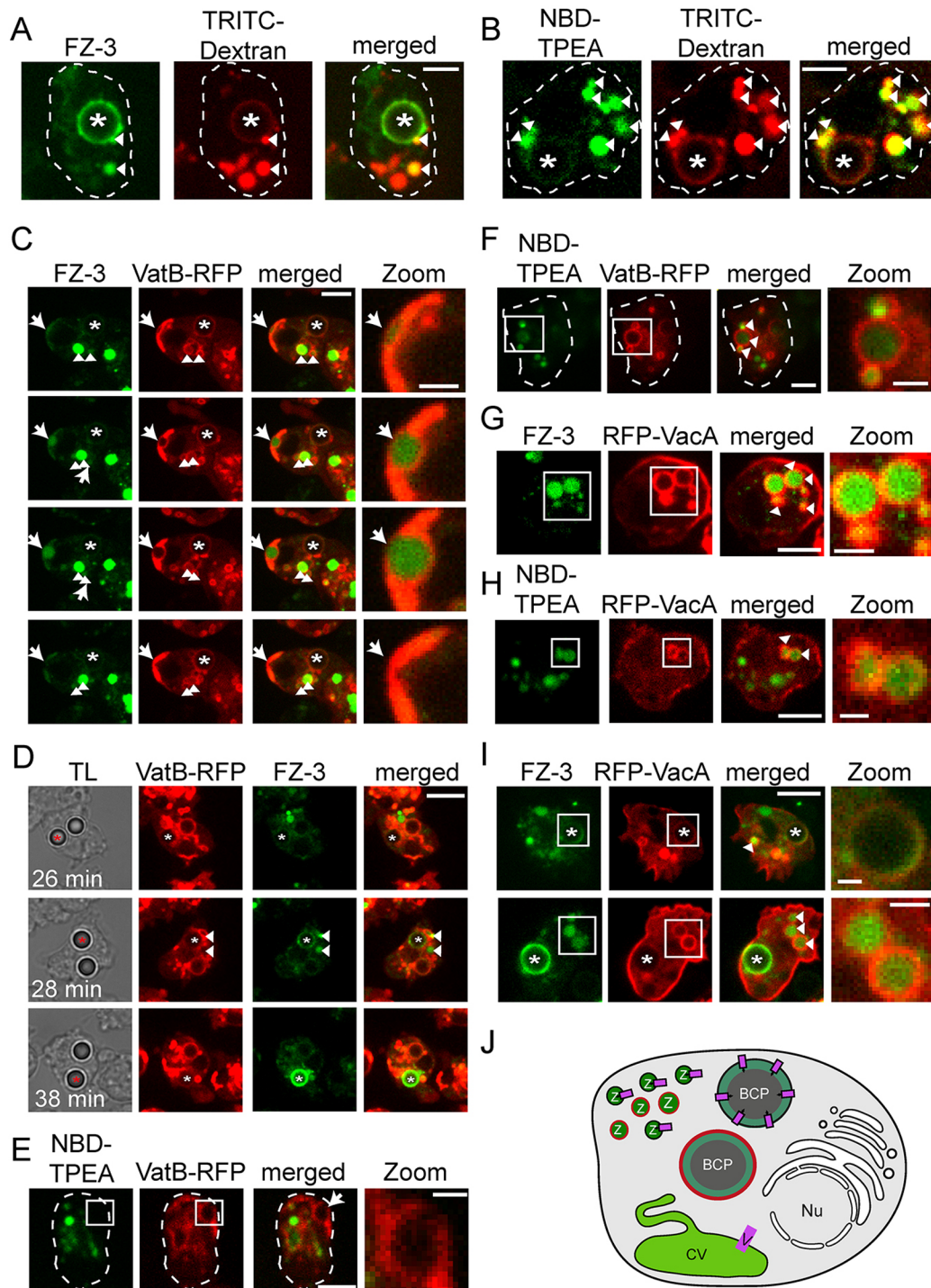


**Fig. 1.  $Zn^{2+}$  accumulates inside the CV network and zincosomes.** (A,B)  $Zn^{2+}$  is observed in the endosomal system. Cells were incubated with TRITC-dextran, stained with FZ-3 (A) or NBD-TPEA (B), and fed with 3  $\mu$ m latex beads. Scale bars: 5  $\mu$ m. (C) Zinc is removed from the cell when the CV discharges. Shown are snapshots from Movie 1. Scale bars: 5  $\mu$ m (zoom 2  $\mu$ m). (D) FZ-3 fluoresces inside a BCP when the vATPase is retrieved. TL, transmitted light. Scale bar: 10  $\mu$ m. (E) There is no NBD-TPEA signal inside the CV. Scale bar: 5  $\mu$ m (zoom 2  $\mu$ m). (F) Zincosomes have partially lysosomal characteristics. Scale bar: 5  $\mu$ m (zoom 2  $\mu$ m). Cells expressing VatB-RFP were stained with FZ-3 (C,D) or NBD-TPEA (E,F) and fed with beads. (G,H) Zincosomes have partially postlysosomal characteristics. Scale bars: 5  $\mu$ m (zoom 2  $\mu$ m). (I)  $Zn^{2+}$  accumulates inside BCPs at the postlysosomal stage. Scale bars: 5  $\mu$ m (zoom 1  $\mu$ m). RFP-VacA-expressing cells were used (F,G,I). Arrowheads point to zincosomes; arrows point to the site of  $Zn^{2+}$  discharge from the CV; asterisks label BCPs. (J) Scheme.  $Zn^{2+}$  accumulates inside the CV network, zincosomes and BCPs in *Dictyostelium*. BCP, bead-containing phagosome; CV, contractile vacuole; Nu, nucleus; v, vATPase; Z, zincosomes. VacA is shown in red.



contributes to the digestion of bacterial components in concert with various sets of lysosomal enzymes that are transferred to the phagosome by fusion with endosomes and lysosomes (Gotthardt et al., 2002). These enzymes are then retrieved from the phagosomes together with the vATPase starting 45 min after uptake, leading to a postlysosomal compartment with neutral luminal pH (Gotthardt et al., 2002). Undigested material is then expelled from the cell by exocytosis. In *Dictyostelium*, free  $Zn^{2+}$  has been recently localized in the contractile vacuole (CV), an organelle crucial for osmoregulation, and in the endolysosomal system, including phagosomes containing nonpathogenic *E. coli* (Buracco et al., 2018).

Here, we monitor free  $Zn^{2+}$  in the endophagocytic pathways of *Dictyostelium*, to compare with knowledge acquired in macrophages, and to understand the evolutionary origin of the metal poisoning strategy. Moreover, so far it remains unclear whether ZnTs are involved in the  $Zn^{2+}$  accumulation in the endosomal-lysosomal pathway and, consequently, we extended our analysis to various *znt* knockouts.

## RESULTS

### In *Dictyostelium*, zincosomes are mainly of lysosomal and postlysosomal nature

To decipher in more detail the recently reported subcellular localization of free  $Zn^{2+}$  in *Dictyostelium* (Buracco et al., 2018), cells were pre-incubated overnight with the fluid-phase tracer tetramethylrhodamine (TRITC)-dextran [which accumulates in all endosomes and lysosomes (Hacker et al., 1997)]. The cells were stained with either FluoZin-3 AM (FZ-3; Fig. 1A) or N1-(7-Nitro-2,1,3-benzoxadiazol-4-yl)-N1,N2,N2-tris(2-pyridinylmethyl)-1,2-ethane-diamine (NBD-TPEA; Fig. 1B), two fluorescent probes selective for  $Zn^{2+}$ , and fed with 3  $\mu$ m latex beads. Importantly, using these two fluorescent probes, we were able to localize  $Zn^{2+}$  inside the different cellular compartments, but not in the cytosol. As revealed by FZ-3 and NBD-TPEA staining (Fig. 1A,B),  $Zn^{2+}$  was clearly detectable inside the bead-containing phagosomes (BCPs, asterisks) and zincosomes that colocalized with the endosomal marker TRITC-dextran (arrowheads). To define more precisely the identity of zincosomes, *Dictyostelium* expressing VatB-RFP, a

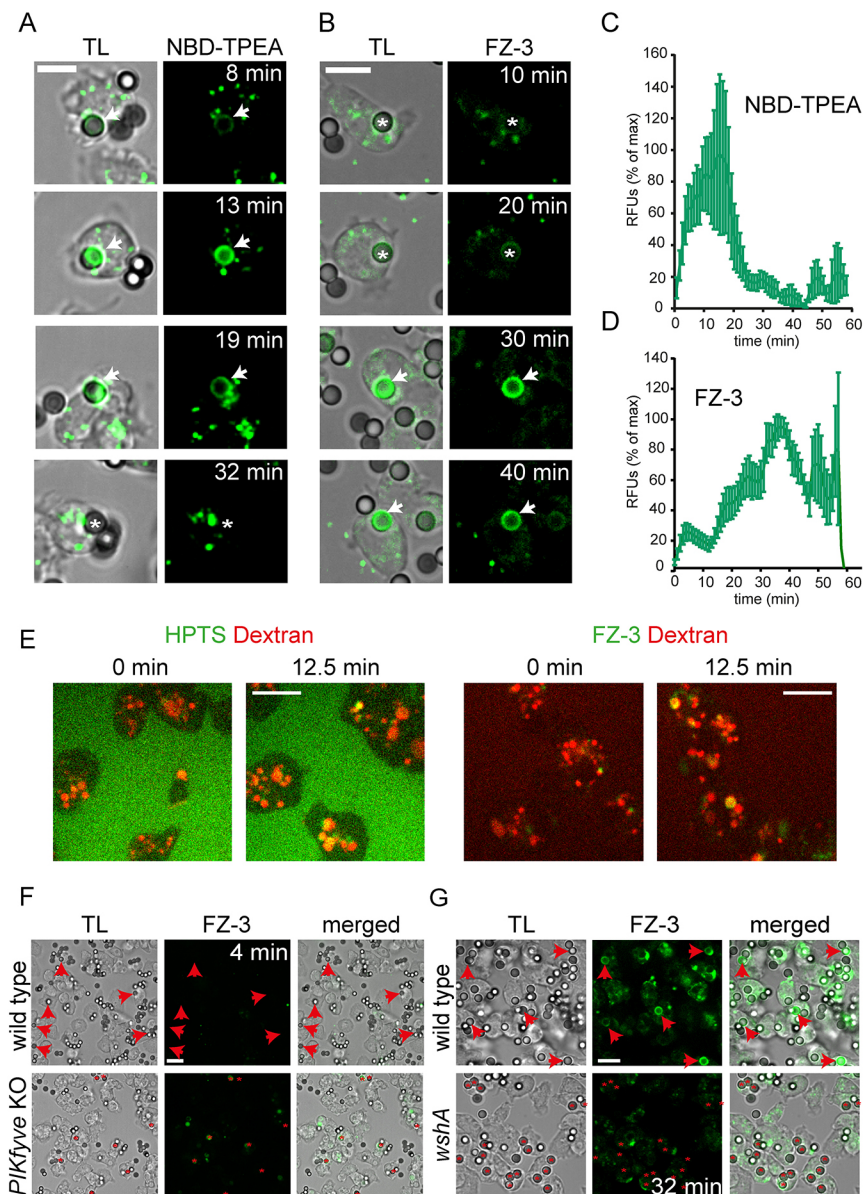


**Fig. 2. Intracellular distribution of  $Zn^{2+}$  during the phagocytic pathway of *Dictyostelium*.** (A–D) After NBD-TPEA (A) or FZ-3 (B) staining, cells were fed with 3  $\mu$ m latex beads. Single beads were followed by live microscopy from uptake to exocytosis (Movies 2 and 3). Scale bars: 5  $\mu$ m. (C,D) Relative fluorescence intensities inside the BCPs were quantified using ImageJ and the 'CenterOnClick' plugin. Eight BCPs per fluorescent probe were quantified. (E) Cells that were treated overnight with 10 kDa fluorescent dextran and HPTS were then incubated with FZ-3. LLOMe was added 2.5 min after a time-lapse movie was started. Scale bar: 10  $\mu$ m. (F,G) *Dictyostelium* wild-type and the *PIKfyve* (F) or *wshA* (G) KO cells were stained with FZ-3 and fed with latex beads. Images were taken 4 min (F) and 32 min (G) after bead addition. Scale bars: 10  $\mu$ m. TL, transmitted light. Asterisks indicate BCPs; arrows point to NBD-TPEA- or FZ-3-positive BCPs.

marker of lysosomes and the CV (Bracco et al., 1997), or RFP-VacA, a marker of postlysosomes (Wienke et al., 2006), were stained with both  $\text{Zn}^{2+}$  probes and fed with latex beads (Fig. 1C–I). Using these markers,  $\text{Zn}^{2+}$  was detected inside bladders of the CV before discharge (Fig. 1C, arrows; Movie 1), in VatB-RFP-positive lysosomes (Fig. 1F, arrowheads) and in VatB-RFP-negative, but RFP-VacA-positive, postlysosomes (Fig. 1D,F–I, arrowheads). Besides its osmoregulatory function and role in  $\text{Ca}^{2+}$  sequestration, the CV is proposed to serve as a transient sink for divalent metals (Bozzaro et al., 2013). Consequently, our observations are in line with the hypothesis that toxic metals and other ions are expelled from the cell via the CV (Bozzaro et al., 2013; Heuser et al., 1993). Importantly, we observed that lysosomes were not labelled by FZ-3 (Fig. 1D; Movie 1), and there was no NBD-TPEA signal inside the CV (Fig. 1E).

Taken together, our data support the localization of  $\text{Zn}^{2+}$  inside zinsosomes that are of lysosomal and postlysosomal nature, as well as inside BCPs and in the CV (Fig. 1J).

### Localization of free $\text{Zn}^{2+}$ during phagocytosis in *Dictyostelium*

We precisely monitored the dynamics of appearance and accumulation of  $\text{Zn}^{2+}$  in the BCP by time-lapse microscopy (Fig. 2A–D). Strikingly, the NBD-TPEA signal became visible inside BCPs very early after uptake, peaked at 15–20 min and then disappeared until the beads were exocytosed (Fig. 2A,C; Movie 2), whereas the FZ-3 signal was first observed only after ~20 min postuptake, peaked at 35–40 min and persisted until exocytosis (Fig. 2B,D; Movie 3). We verified that the two probes were specific for  $\text{Zn}^{2+}$ , because the signals of both NBD-TPEA and FZ-3 were eliminated by TPEN [N,N,N',N'-tetrakis-(2-pyridylmethyl)-ethylenediamine], a cell-permeant  $\text{Zn}^{2+}$  chelator, but not by the nonpermeant  $\text{Zn}^{2+}$  chelator diethylenetriaminepentaacetic acid (DTPA; Fig. S1A,B).

It is known that a pH lower than 5 quenches by ~50% the FZ-3 signal, whereas a pH lower than 4 leads to a complete extinction of

the FZ-3 signal (Gee et al., 2002). On the contrary, NBD-TPEA is not affected by low pH, but quenched by  $\text{Cu}^{2+}$  concentrations of ~30  $\mu\text{M}$  (Xu et al., 2009). The phagosomes of *Dictyostelium*, more acidic than those in macrophages (Yates et al., 2005), reach a pH lower than 3.5 a few minutes after particle uptake (Marchetti et al., 2009; Sattler et al., 2013), which could explain the fact that, in wild-type cells, most of the BCPs became FZ-3 fluorescent only after ~30 min of bead uptake (Fig. 2B,D). To demonstrate that the absence of FZ-3 signal in endosomes and lysosomes is due to low pH, cells stained with FZ-3 and 10 kDa dextran were incubated with the lysosome-disrupting agent L-leucyl-L-leucine methyl ester (LLOMe) as described previously (Lopez-Jimenez et al., 2018). LLOMe creates small pores, leading to proton leakage and re-neutralization of the compartments (Repnik et al., 2017). This can be monitored directly with the help of the pH-dependent dye 8-hydroxypyrene-1,3,6-trisulfonic acid (HPTS) (Fig. 2E, left). In the case of FZ-3, addition of LLOMe resulted in an acute and drastic increase of the FZ-3 signal in most vesicles (Fig. 2E, right), confirming our hypothesis. To further assess whether low pH is also responsible for the absence of FZ-3 signal in the early BCPs of wild-type cells, we fed latex beads to *PIKfyve* knockout (KO) cells, which are strongly inhibited in phagosomal acidification (Buckley et al., 2018). As shown in Fig. 2F, BCPs became FZ-3 positive only few minutes after uptake, and remained brightly fluorescent until exocytosis. In sharp contrast, the BCPs of *wshA* mutant cells, which are incapacitated in re-neutralizing phagosomes due to a defect in the retrieval of the vATPase (Carnell et al., 2011), did not show any FZ-3 fluorescence (Fig. 2G). These results confirm that FZ-3 is quenched in early BCPs, owing to the low luminal pHs, and becomes fluorescent only during re-neutralization, when the vATPase is retrieved (Fig. 1D). Regarding the sensitivity of NBD-TPEA to  $\text{Cu}^{2+}$ , cells were pre-treated with different concentrations of  $\text{CuSO}_4$  before incubation with the probe and beads. Five  $\mu\text{M}$   $\text{CuSO}_4$  was sufficient to completely quench the signal of NBD-TPEA inside BCPs (Fig. S1C), indicating that its fluorescence is likely quenched by the import of  $\text{Cu}^{2+}$  into maturing

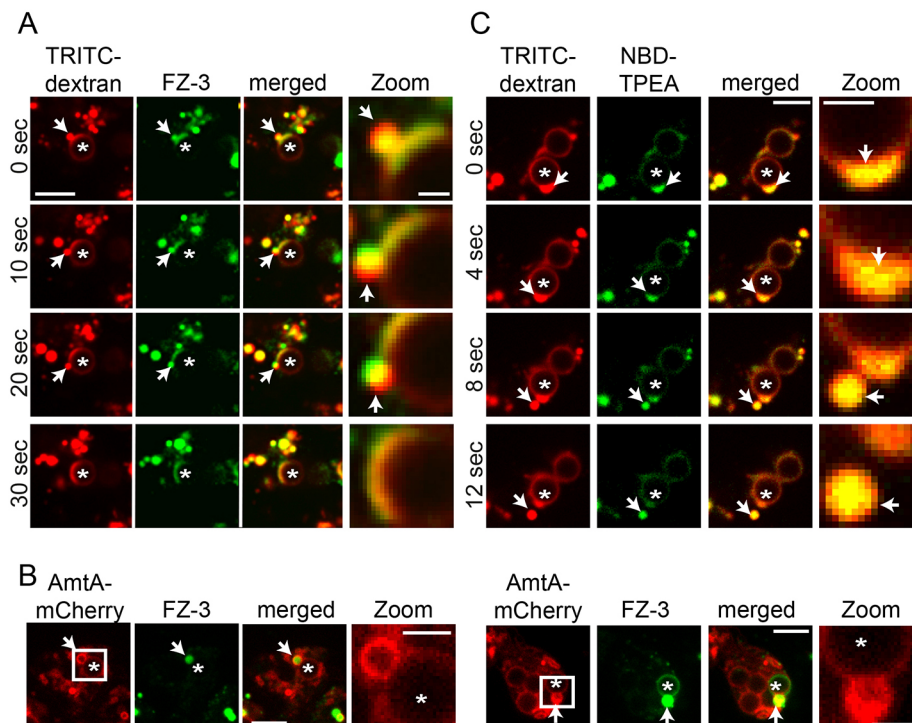


**Fig. 3. Fusion and fission dynamics of zinsosomes at BCPs.** (A) Cells were incubated with TRITC-dextran overnight, stained with FZ-3 and fed with 3  $\mu\text{m}$  latex beads. Scale bar: 5  $\mu\text{m}$  (zoom 1  $\mu\text{m}$ ). Shown are snapshots from time-lapse Movie 4. (B) Cells expressing AmtA-mCherry were stained with FZ-3 and fed with beads. Shown are two examples of AmtA-positive zinsosomes fusing with BCPs. Scale bar: 5  $\mu\text{m}$  (zoom 1  $\mu\text{m}$ ). (C) Cells were treated as in A, but stained with NBD-TPEA. Scale bar: 3  $\mu\text{m}$  (zoom 1  $\mu\text{m}$ ). Shown are snapshots from time-lapse Movie 5. Asterisks mark BCPs; arrows label the zinsosome-phagosome fusion site (A,B) or the zinsosome-phagosome budding site (C).



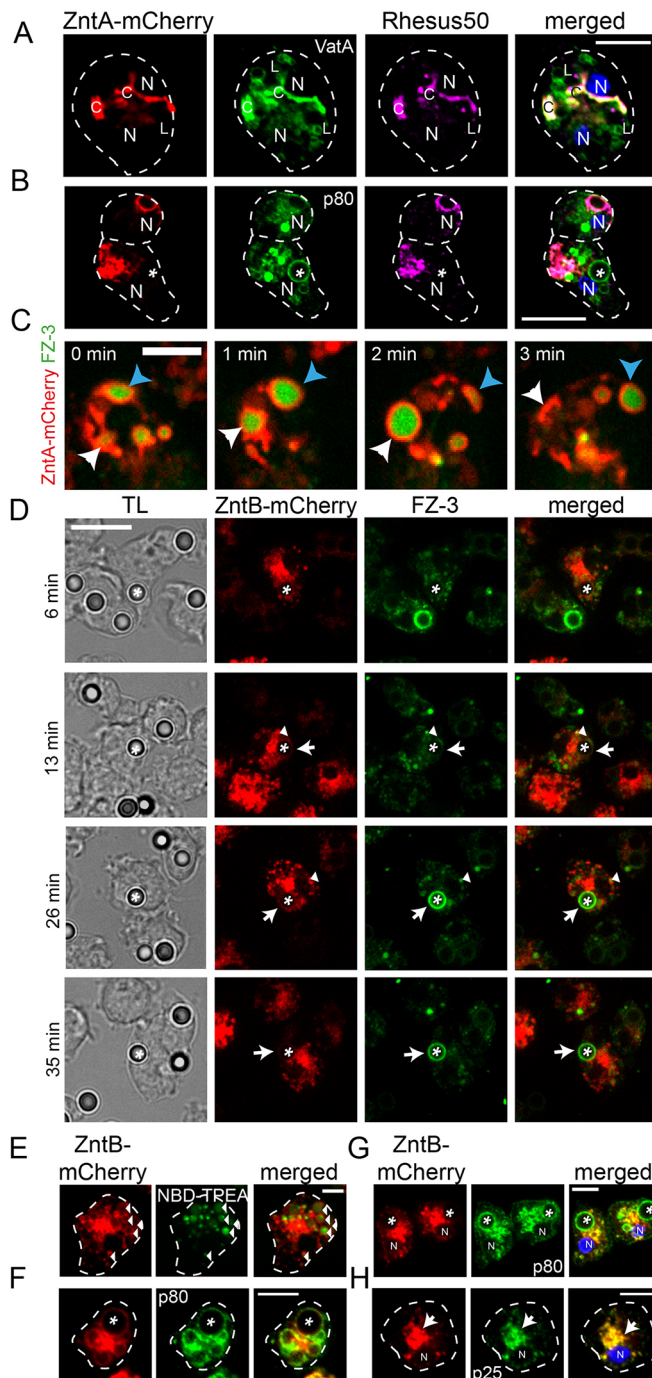


**Fig. 4. Subcellular localization of ZntA and ZntB.** (A,B) ZntA colocalizes with the CV markers Rhesus50 and VatA, but not with the endosomal protein p80. ZntA-mCherry-expressing cells were fixed and stained with antibodies against Rhesus50 (A,B), VatA (A) and p80 (B). The signal from ZntA-mCherry was enhanced with an anti-RFP antibody. Nuclei were stained with DAPI. C, tubular network of the CV; N, nucleus; L, lysosome. Asterisks label BCPs. Scale bars: 5  $\mu$ m (A) and 10  $\mu$ m (B). (C)  $Zn^{2+}$  is enriched at ZntA-labelled CV compartments. ZntA-mCherry-expressing cells were stained with FZ-3. Scale bar: 5  $\mu$ m. Arrowheads point to the sites of CV discharge. (D) ZntB is recruited to BCPs during phagosome maturation. Shown are images from a time-lapse movie (Movie 6). Scale bar: 15  $\mu$ m. (E) ZntB localizes at zincosomes. Images were taken live. Scale bar: 2  $\mu$ m. Cells expressing ZntB-mCherry were stained with FZ-3 (D) or NBD-TPEA (E) and fed with 3  $\mu$ m latex beads. Asterisks label BCPs; arrows point to a ZntB-positive BCP; arrowheads label ZntB-mCherry-positive zincosomes. (F–H) ZntB colocalizes with endosomal markers. ZntB-mCherry-expressing cells were fixed and stained with antibodies against p80 (F,G) and p25 (H). The signal from ZntB-mCherry was enhanced with an anti-RFP antibody. Nuclei were stained with DAPI. Asterisks label BCPs; the arrow points to a clustering of ZntB-mCherry at the juxtannuclear region. N, nucleus. Scale bars: 5  $\mu$ m.

pre-incubation with TRITC-dextran, staining with FZ-3 or NBD-TPEA, and feeding with 3  $\mu$ m latex beads) revealed that zincosomes observed in the vicinity of the BCP (asterisks) can sometimes be captured in the process of fusion, during which they deliver their content into the BCP lumen, leading to a crescent shape that increased and spread over time (Fig. 3A; Movie 4, arrows). These observations suggest that  $Zn^{2+}$  is delivered to maturing BCPs via zincosome-phagosome fusion. Interestingly, a large fraction of the delivering zincosomes was surrounded by AmtA, an ammonium transporter present in endosomes and phagosomes (Kirsten et al., 2008; Uchikawa et al., 2011), confirming their endosomal nature (Fig. 3B). We also observed that  $Zn^{2+}$  was present in zincosomes formed by scission of a vesicle from NBD-TPEA-positive BCPs (Fig. 3C; Movie 5, arrows). In summary, the dynamic relationship between zincosomes and BCPs is complex. Our experiments clearly show that  $Zn^{2+}$  can be delivered by zincosome-BCP fusion, although it has not yet been possible to quantitate the contribution of this pathway to the total phagosomal  $Zn^{2+}$  concentration.

#### Subcellular localization of ZnTs in *Dictyostelium*

$Zn^{2+}$  is sequestered into cellular organelles by  $Zn^{2+}$  transporters of the ZnT family (Kambe et al., 2015). In order to determine the localization of the *Dictyostelium*  $Zn^{2+}$  transporters, cells expressing fluorescent chimeras of each of the four ZnT proteins were fixed and stained with antibodies against several CV and endosomal markers (Figs 4 and 5). ZntA-mCherry partially colocalized with VatA, a subunit of the vATPase present in both lysosomes and membranes of the CV network (Neuhaus et al., 1998), and perfectly colocalized with Rhesus50, a protein that localizes exclusively to the CV (Benghezal et al., 2001) (Fig. 4A).

To monitor whether ZntA-mCherry might additionally localize to phagosomes at some stage of maturation, cells were fed with latex beads, fixed and stained with an antibody against p80 (Fig. 4B), a predicted Cu transporter that is located throughout the endosomal pathway and concentrates at postlysosomes (Ravanel et al., 2001). These experiments excluded colocalization of ZntA and p80 (Fig. 4B), and highlighted that ZntA-mCherry was, in fact, not detected in BCPs (Fig. S2, asterisks). To confirm the exclusive presence of ZntA at CV membranes, live microscopy was performed on ZntA-mCherry-expressing cells incubated with FZ-3. The fluorescent probe accumulated in ZntA-positive bladders of the CV that frequently discharged their content, expelling FZ-3-chelated  $Zn^{2+}$  to the extracellular milieu (Fig. 4C,

BCPs. Altogether, integrating the information acquired with both dyes (Figs 1 and 2; Fig. S1), we conclude that free  $Zn^{2+}$  is in fact present inside BCPs from early stages after bead uptake and until exocytosis of the particle. In addition, FZ-3 and NBD-TPEA can be used in combination with fluorescent organelle reporters to decipher the localization and function of  $Zn^{2+}$  during grazing on bacteria.

#### $Zn^{2+}$ can be delivered to phagosomes by fusion with endolysosomal compartments

In macrophages,  $Zn^{2+}$  can be delivered to phagosomes via fusion with endosomes (Botella et al., 2011). We wondered whether this was also the case in *Dictyostelium*. Careful examination of amoebae during the phagocytosis assays mentioned above (i.e.

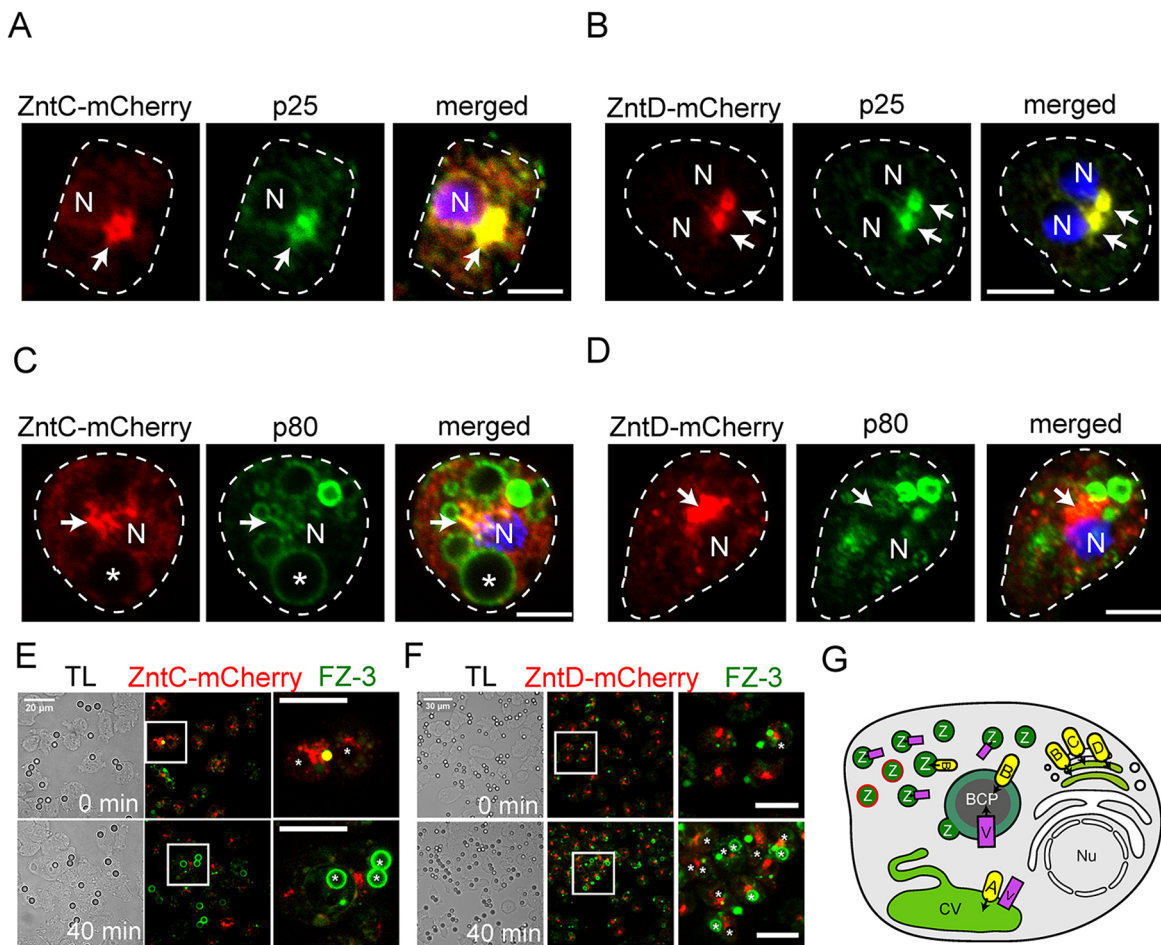


**Fig. 5. Subcellular localization of ZntC and ZntD.** (A,B) ZntC-mCherry (A) and ZntD-mCherry (B) are localized in the juxtanuclear region. (C,D) ZntC-mCherry (C) and ZntD-mCherry (D) do not colocalize with the endosomal marker p80. Cells were fixed and stained with antibodies against p80 and p25. Nuclei were stained with DAPI. The signal from ZntC- and ZntD-mCherry was enhanced with an anti-RFP antibody. Asterisks label BCPs; arrows point to enrichment of ZntC- or ZntD-mCherry at the juxtanuclear region. N, nucleus. Scale bars: 5  $\mu$ m. (E,F) ZntC- and ZntD-mCherry do not colocalize with BCPs. Cells were stained with FZ-3 and fed with 3  $\mu$ m latex beads. Shown are images from time-lapse movies. Asterisks label BCPs. Scale bars: 20  $\mu$ m (E) and 30  $\mu$ m (F) (zoom 15  $\mu$ m). (G) Scheme summarizing the subcellular localization of ZnTs in *Dictyostelium*. A, ZntA; B, ZntB; BCP, bead-containing phagosome; C, ZntC; CV, contractile vacuole; D, ZntD; Nu, nucleus; v, vATPase; Z, zincosomes. VacA is shown in red.

arrowheads). Therefore, we conclude that ZntA is located exclusively to the CV bladders and network.

Using the same approach, cells expressing ZntB-mCherry and incubated with FZ-3 were fed latex beads, revealing the presence of ZntB-mCherry at BCPs (Fig. 4D, asterisks), starting from 6 min to until 35 min after bead uptake (Fig. 4D, arrows; Movie 6). In addition, ZntB-mCherry was also observed around FZ-3-positive zincosomes (Fig. 4D, arrowheads). The ZntB-mCherry-labelled zincosomes (Fig. 4E, arrowheads) and BCPs (Fig. S3A, asterisks) were also positive for NBD-TPEA, indicating that the ZntB-positive compartments can be acidic and likely contain a relatively low  $\text{Cu}^{2+}$  concentration. In addition, ZntB-mCherry partially colocalized with p80 at BCPs (Fig. 4F,G), indicating their lysosomal or early postlysosomal nature. This is in line with the observation that ZntB-mCherry also colocalized with the vATPase (Fig. S3B), but not with Rhesus50 or the endoplasmic reticulum marker PDI (Fig. S3C,D). Similar to its human homologue ZNT10 (also known as SLC30A10) (Bosomworth et al., 2012; Dunn et al., 2018), ZntB was also located at recycling endosomes and/or the Golgi complex, as determined by its juxtanuclear colocalization with p25, a marker for recycling endosomes (Charette et al., 2006) (Fig. 4H). Note that, in *Dictyostelium*, recycling endosomes concentrate around the

microtubule organizing centre (MTOC), a region in which, typically, the Golgi complex is also located. These results led us to conclude that ZntB locates mainly to organelles of the endosomal pathway.

To decipher the subcellular localization of ZntC and ZntD, homologues of human ZNT6 (also known as SLC30A6) and ZNT7 (also known as SLC30A7), respectively (Dunn et al., 2018), cells expressing ZntC- and ZntD-mCherry were fixed and stained with antibodies against p80 and p25. ZntC- and ZntD-mCherry both colocalized with p25 in the juxtanuclear region (Fig. 5A,B), and did not colocalize significantly with p80 (Fig. 5C,D), suggesting that these transporters either locate in recycling endosomes that are usually low in p80 (Charette et al., 2006), or in the Golgi complex. Importantly, ZntC- and ZntD-mCherry were not observed at BCPs at any stage of maturation (Fig. 5E,F). The locations of the various *Dictyostelium* ZnTs are schematized in Fig. 5G.

#### ZntA is the main $\text{Zn}^{2+}$ transporter of the CV

$\text{Zn}^{2+}$  accumulates inside the CV and is expelled from the cell when the CV discharges (Figs 1C and 4C). Because ZntA was the only ZnT localized at the CV membrane (Fig. 4A–C; Fig. S2), we wondered whether ZntA was involved in the import of  $\text{Zn}^{2+}$  into



the CV lumen. To test this hypothesis, a *zntA* KO was created (see Materials and Methods and Fig. S4A,B), and wild-type and *zntA* KO cells expressing VatB-RFP were incubated with 3  $\mu$ m latex beads and FZ-3 (Fig. 6A,B). As expected, the FZ-3 signal was visible in BCPs of wild-type and mutant cells (Fig. 6A,B);

however, no signal was observed in the VatB-RFP-positive CV of *zntA* KO cells (Fig. 6B). This suggests that ZntA mediates the main route of  $Zn^{2+}$  delivery into the CV. Overexpressing mCherry-ZntA in *zntA* KO cells rescued the transport of  $Zn^{2+}$  inside the CV network (Fig. 6C). Interestingly, when cells expressing

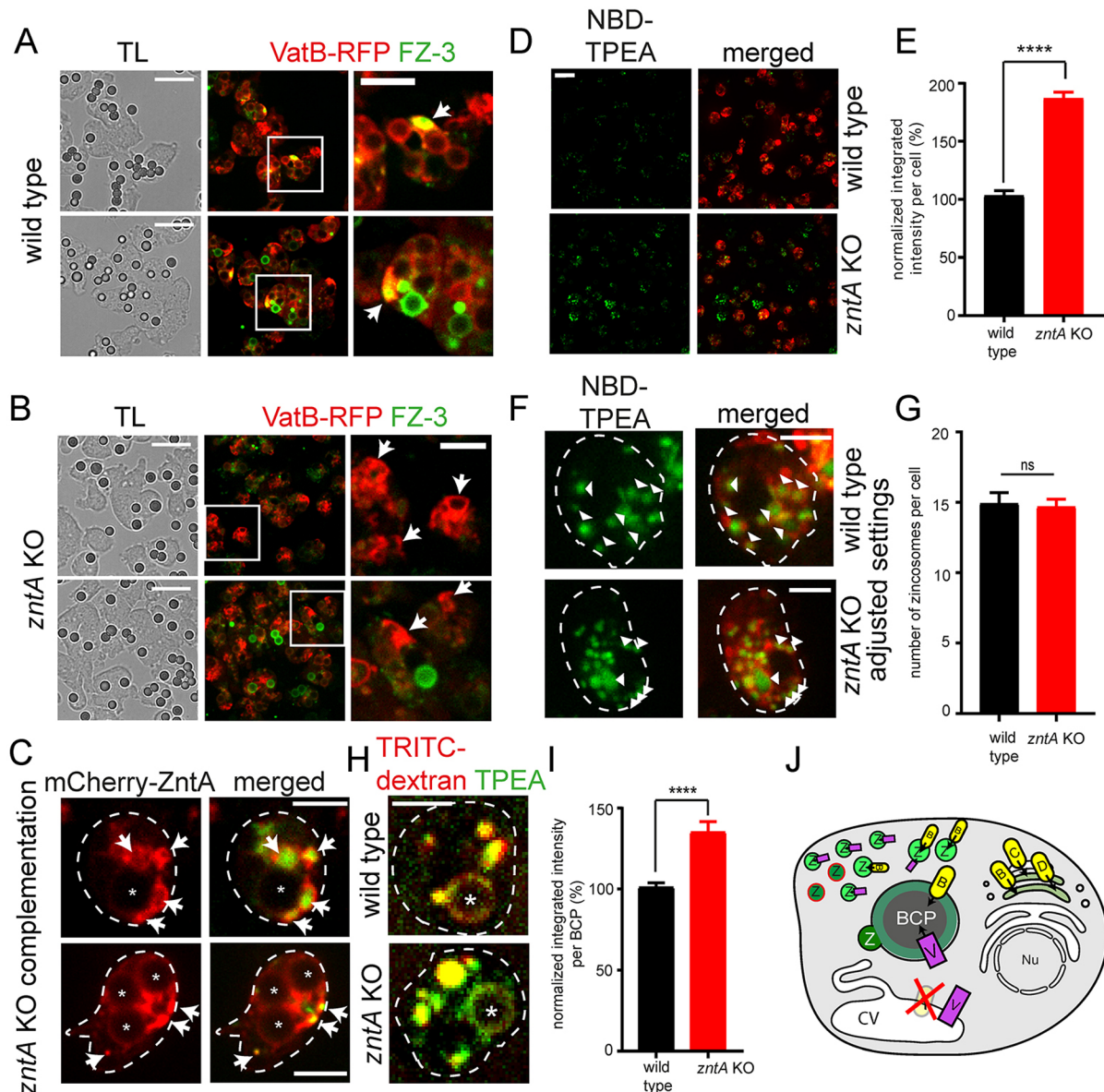


**Fig. 6. ZntA is the main  $Zn^{2+}$  transporter of the CV.** (A,B)  $Zn^{2+}$  is absent from the CV network of the *zntA* KO. Shown are pictures from time-lapse movies taken at 8 min (top row) and 50 min (bottom row) after the experiment was started. Scale bars: 20  $\mu$ m (zoom 10  $\mu$ m). (C) Overexpression of mCherry-ZntA rescues the phenotype of the *zntA* KO. Scale bars: 5  $\mu$ m. Wild-type (A) and *zntA* KO cells (B) expressing VatB-RFP or *zntA* KO cells expressing mCherry-ZntA (C) were fed with 3  $\mu$ m latex beads and stained with FZ-3. Arrows point to CV bladders filled with  $Zn^{2+}$  in the wild type or mCherry-ZntA overexpressor and to empty CV bladders in the *zntA* KO; asterisks label BCPs. (D) Mislocalized  $Zn^{2+}$  is shuttled into acidic zinsosomes in the *zntA* KO. Cells expressing AmtA-mCherry were stained with NBD-TPEA. Images were taken by live microscopy. Scale bar: 10  $\mu$ m. (E) Quantification of D. The total integrated density per cell was quantified using ImageJ. Statistical significance was calculated with an unpaired Student's *t*-test (\*\*\*\* $P$ <0.0001). Bars represent the mean $\pm$ s.e.m. of four independent experiments. 130 cells were analysed for the wild type and 121 cells were analysed for the *zntA* KO. (F) Same as in D, but the microscope settings were adjusted to compare the number of zinsosomes in wild type and *zntA* KO. Arrowheads point to zinsosomes. Scale bars: 5  $\mu$ m. (G) The number of zinsosomes remains unchanged in the *zntA* KO. The number of zinsosomes in wild type and *zntA* KO was counted using MetaXpress. More than 767 cells were analysed per experiment and condition. Statistical significance was calculated with an unpaired Student's *t*-test. Bars represent the mean $\pm$ s.d. of three independent experiments. ns, nonsignificant. (H)  $Zn^{2+}$  accumulates inside the BCPs of the *zntA* KO. Scale bar: 5  $\mu$ m. (I) Quantification of H. The integrated density inside the BCPs was quantified using ImageJ. Statistical significance was calculated with an unpaired Student's *t*-test (\*\*\*\* $P$ <0.0001). Bars represent the mean $\pm$ s.e.m. of three independent experiments. 127 BCPs were analysed for the wild type and 106 BCPs were analysed for the *zntA* KO. (J) Summarizing scheme showing the mislocalization of  $Zn^{2+}$  in the *zntA* KO. A, ZntA; B, ZntB; BCP, bead-containing phagosome; C, ZntC; CV, contractile vacuole; D, ZntD; Nu, nucleus; v, vATPase; Z, zinsosomes. VacA is shown in red.

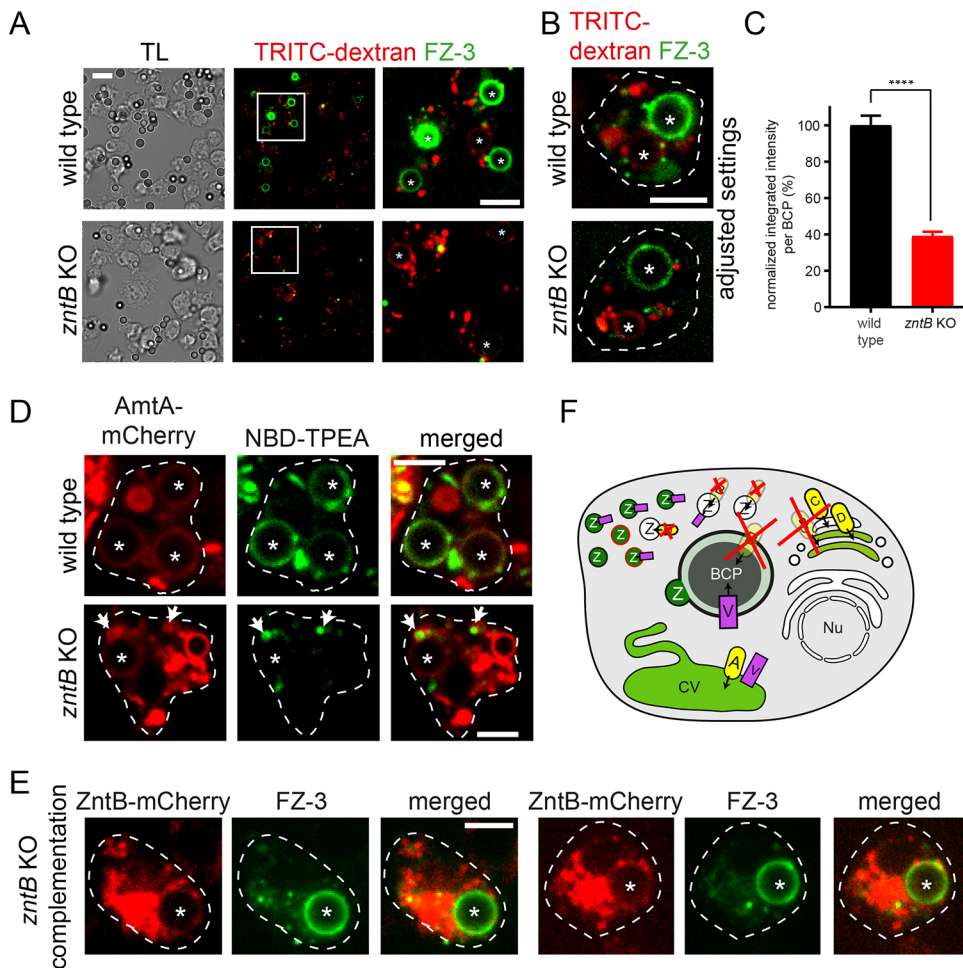


**Fig. 7. ZntB is the main endosomal Zn<sup>2+</sup> transporter.** (A–D) Zn<sup>2+</sup> is almost absent from BCPs in the *zntB* KO. (A) Cells were incubated overnight with TRITC-dextran, co-stained with FZ-3 and fed with 3  $\mu$ m latex beads. Scale bar: 10  $\mu$ m (zoom 5  $\mu$ m). (B) Same as in A. To show the residual amount of Zn<sup>2+</sup> inside the BCPs of the *zntB* KO, the brightness and contrast of the image was adjusted using ImageJ. Scale bar: 5  $\mu$ m. (C) Quantification of A. The integrated density inside the BCPs was quantified using ImageJ. Statistical significance was calculated with an unpaired Student's *t*-test (\*\*\*\**P*<0.0001). Bars represent the mean $\pm$ s.e.m. of three independent experiments. 103 BCPs were analysed for the wild type and 93 BCPs were analysed for the *zntB* KO. (D) Cells expressing AmtA-mCherry were stained with NBD-TPEA and fed with 3  $\mu$ m latex beads. Scale bars: 5  $\mu$ m. (E) The phenotype of the *zntB* KO is rescued by overexpression of ZntB-mCherry. *ZntB* KO cells expressing ZntB-mCherry were incubated with FZ-3 and fed with 3  $\mu$ m latex beads. Scale bar: 5  $\mu$ m. Arrows point to zincosomes; asterisks label BCPs. (F) Summarizing scheme showing the absence of Zn<sup>2+</sup> in the BCPs of the *zntB* KO. A, ZntA; B, ZntB; BCP, bead-containing phagosome; C, ZntC; CV, contractile vacuole; D, ZntD; Nu, nucleus; v, vATPase; Z, zincosomes.

AmtA-mCherry were stained with NBD-TPEA, the intensity of the signal in zincosomes of the *zntA* KO was more intense than in wild-type cells (Fig. 6D,E). Importantly, knocking out *zntA* did not alter the number of zincosomes (Fig. 6F,G). By quantifying the integrated signal intensity inside BCPs, we observed a higher level of zinc inside the phagosomes of *zntA* KO cells compared with wild type (Fig. 6H,I).

In conclusion, these data indicate that ZntA is the main Zn<sup>2+</sup> transporter of the CV system, and that the absence of ZntA leads to an increased concentration of Zn<sup>2+</sup> in the endosomal system (Fig. 6J).

### ZntB is the main lysosomal and postlysosomal Zn<sup>2+</sup> transporter

As mentioned above, ZntB localized at zincosomes and phagosomes (Fig. 4D–H; Fig. S3). To test whether ZntB mediates the transport of Zn<sup>2+</sup> into these compartments, a *zntB* KO, generated within the Genome Wide *Dictyostelium* Insertion (GWDI) project, was used (Fig. S4C). The insertion site of the blasticidin cassette was confirmed by genomic PCR (Fig. S4D). Wild-type and *zntB* KO cells were incubated overnight with TRITC-dextran, stained with FZ-3 or NBD-TPEA, and fed with 3  $\mu$ m latex beads (Fig. 7A–D). Strikingly, both FZ-3 and NBD-TPEA signals in the BCPs of *zntB* KO cells appeared strongly reduced (Fig. 7A,D). By adjusting the image settings, and by quantification of the integrated signal intensity inside BCPs, the signal in *zntB* KO cells was shown to be decreased by ~60% compared with wild type (Fig. 7B,C). The residual amount of Zn<sup>2+</sup> detected might be delivered to BCPs by fusion with zincosomes that are also present in

the *zntB* KO (Fig. 7D, arrows). Importantly, overexpression of ZntB-mCherry in the *zntB* KO rescued the defect in Zn<sup>2+</sup> content (Fig. 7E).

We propose that ZntB is the main Zn<sup>2+</sup> transporter in lysosomes and postlysosomes (Fig. 7F), and that, in its absence, residual levels of Zn<sup>2+</sup> are reached within these compartments by fusion with zincosomes or trafficking from recycling endosomes, where Zn<sup>2+</sup> is transported by ZntC or ZntD.

As ZntB is located at BCPs, a generic type of phagosomes that have a relatively transient nature, leading to particle exocytosis after about 60 min, we wondered whether ZntB is also present at compartments containing the nonpathogenic *Mycobacterium smegmatis*, which are documented to have phagolysosomal identity but are more persistent, releasing killed bacteria after a couple of hours. ZntB-mCherry localized at the membrane of the MCV immediately after bacteria uptake, and Zn<sup>2+</sup>, detected by NBD-TPEA, also accumulated inside the MCV at the same time (Fig. S5). The concentration of intraphagosomal Zn<sup>2+</sup> appeared to increase during the early stages of infection (from 1 min to 33 min postuptake), which agrees with the hypothesis of ZntB being the main lysosomal Zn<sup>2+</sup> transporter. Strikingly, as we observed before for BCPs (Fig. 7D), Zn<sup>2+</sup> could also be delivered to the MCV by fusion of ZntB-mCherry-decorated zincosomes (Fig. S5, 33 min).

### Zn<sup>2+</sup> poisoning contributes to the killing of phagocytosed bacteria

In macrophages, infection with *E. coli* leads to an increase in the cytosolic level of Zn<sup>2+</sup>, followed by its transport inside phagosomes (Botella et al., 2011). When *Dictyostelium* was infected with *E. coli*,



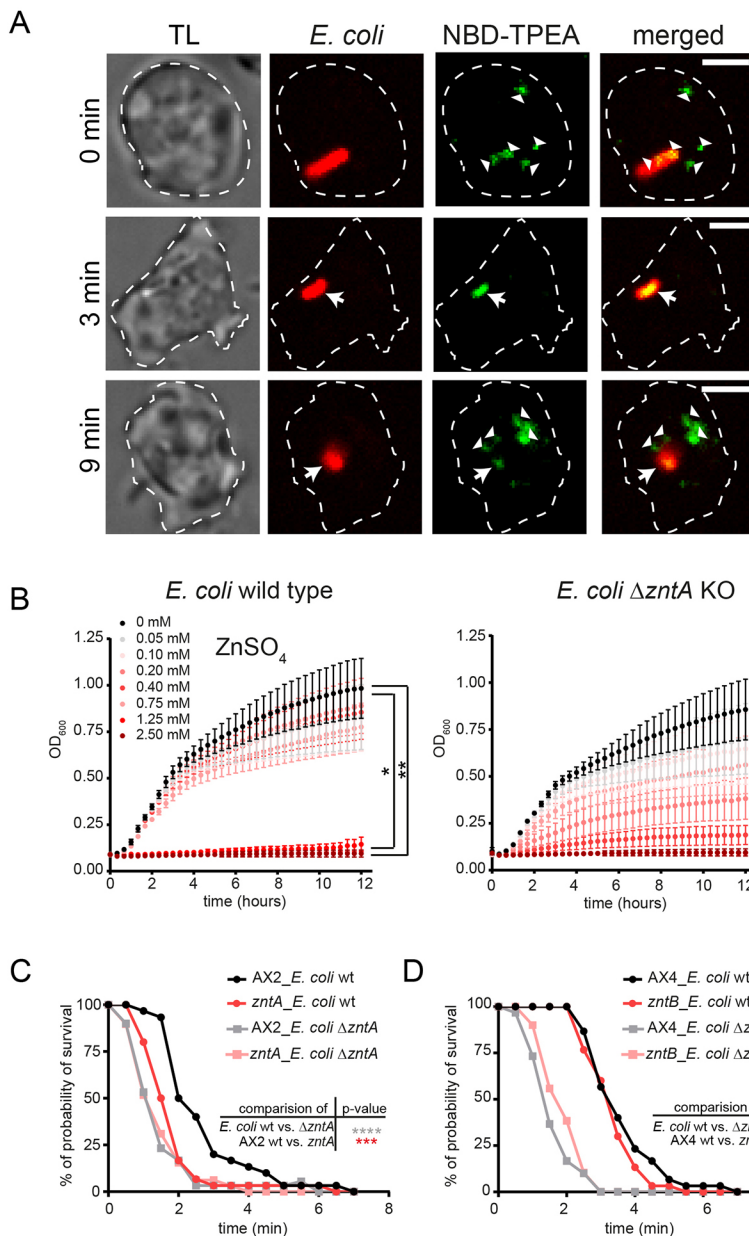


**Fig. 8.  $Zn^{2+}$  poisoning is a killing strategy of *Dictyostelium*.**

(A)  $Zn^{2+}$  accumulates in *E. coli*-containing phagosomes. Cells were incubated with NBD-TPEA and fed with CF594-labelled bacteria before live imaging. Scale bars: 5  $\mu m$ . Arrows point to phagosomes; arrowheads label zincosomes. (B) An *E. coli*  $\Delta zntA$  mutant is more sensitive to increasing concentrations of  $ZnSO_4$  than the wild type. *E. coli* strains were incubated in LB medium.  $ZnSO_4$  was added as indicated. The OD<sub>600</sub> was measured with a 96-well plate reader (SpectraMax i3, Molecular Devices). Statistical differences were calculated with a Bonferroni post hoc test after two-way ANOVA (\* $P < 0.05$ , \*\* $P < 0.01$ ). (C) Bacteria are killed more efficiently by the *Dictyostelium*  $zntA$  KO. (D) Knockout of  $ZntB$  does not affect bacteria killing. *Dictyostelium* was added to wild-type and  $\Delta zntA$  *E. coli* immobilized on an imaging slide with poly-L-lysine and a time-lapse movie was recorded at 30 s intervals. For the Kaplan–Meier survival curves, the data of three independent experiments were combined. 30 ingested bacteria were monitored per condition. The statistical significance was calculated with a log-rank test (\*\*\* $P = 0.0008$ , \*\*\*\* $P < 0.0001$ ).

we could not observe a cytosolic burst of  $Zn^{2+}$ , but  $Zn^{2+}$  appeared in the phagosomes rapidly after uptake (Fig. 8A). This was due, at least in part, to fusion of the phagosomes with zincosomes (Fig. 8A, arrowheads) in line with our previous observations (Fig. 3A; Fig. S5) and the findings in macrophages (Botella et al., 2011).

To determine whether  $Zn^{2+}$  contributes to intraphagosomal bacteria killing by *Dictyostelium*, a  $Zn^{2+}$ -hypersensitive *E. coli* mutant with an inactivated P<sub>1B</sub>-type  $Zn^{2+}$  efflux ATPase [ $\Delta zntA$  (Rensing et al., 1997)] was used. We first confirmed the hypersensitivity of this mutant to  $Zn^{2+}$  (Fig. 8B); 0.2 mM  $Zn^{2+}$  was enough to strongly inhibit its growth *in vitro*, whereas the proliferation of wild-type bacteria was only inhibited by concentrations of  $Zn^{2+}$  above 1.25 mM (Fig. 8B). This differential and dose-dependent inhibition of bacteria growth was not observed for  $Fe^{2+}$  and  $Mn^{2+}$ . The response to  $Cu^{2+}$  was biphasic. Low concentrations led to a weak dose-dependent effect, and higher concentrations fully inhibited growth. Nevertheless, both wild type and  $\Delta zntA$  behaved similarly, and no differential effect of  $Cu^{2+}$  was

observed (Fig. S6A–C). In line with observations in macrophages (Botella et al., 2011), *Dictyostelium* killed the  $\Delta zntA$  mutant bacteria faster than the wild-type *E. coli* (Fig. 8C,D). Interestingly, both *E. coli* strains were killed faster by the *Dictyostelium*  $zntA$  KO than by wild-type *Dictyostelium* (Fig. 8C), whereas no significant difference in killing was observed between *Dictyostelium* wild-type and  $zntB$  KO cells (Fig. 8D). This suggests that accumulation of  $Zn^{2+}$  in the phagolysosomes contributes to bacterial killing and that these compartments harbour a higher  $Zn^{2+}$  concentration in the  $zntA$  KO than in wild-type *Dictyostelium*.

## DISCUSSION

Intracellular bacteria and pathogens are limited to nutrients that are available inside the host cell. Professional phagocytes are able to exploit this dependence and have developed strategies to restrict intracellular bacteria growth or killing. For instance, essential nutrients such as Fe and  $Zn^{2+}$  are either withheld from the pathogen-containing vacuole or pumped into the phagosomal lumen to ensure

bacteria killing in concert with other immunity factors. Nramp1 mediates  $\text{Fe}^{2+}$  sequestration from the phagosome and leads consequently to the starving of the phagosomal bacteria (Bozzaro et al., 2013; Peracino et al., 2006). Surprisingly, both nutrient deprivation (Djoko et al., 2015; Kehl-Fie and Skaar, 2010; Subramanian Vignesh et al., 2013) and metal poisoning have been reported in the case of  $\text{Zn}^{2+}$  (Botella et al., 2011; McDevitt et al., 2011; Soldati and Neyrolles, 2012). Here, we investigated the subcellular localization and role of  $\text{Zn}^{2+}$  in phagocytosis and killing using *Dictyostelium* as a model professional phagocyte.

Inside cells,  $\text{Zn}^{2+}$  is either bound to proteins or sequestered as free  $\text{Zn}^{2+}$  into the various cellular compartments or vesicles. In mammals, 50% of the total cellular  $\text{Zn}^{2+}$  is present in the cytoplasm, 30–40% is in the nucleus and 10% is located at the plasma membrane (Kambe et al., 2015). The cytosolic  $\text{Zn}^{2+}$  concentration ranges from pM to low nM (Vinkenborg et al., 2009).

By using two fluorescent probes, FZ-3 and NBD-TPEA, we investigated the cellular distribution of compartmentalized free  $\text{Zn}^{2+}$  in the professional phagocyte *Dictyostelium*. In line with previous observations from Buracco and colleagues (Buracco et al., 2018),  $\text{Zn}^{2+}$  located inside the endolysosomal system and, more precisely, inside zincosomes of lysosomal and postlysosomal nature (Fig. 1E–J), as well as inside the CV network (Figs 1C and 4C). In addition,  $\text{Zn}^{2+}$  was present in the lumen of phagosomes soon after bead uptake and until exocytosis (Fig. 2A–D). Free  $\text{Zn}^{2+}$  is delivered to maturing phagosomes both via direct pumping and via zincosome fusion (Fig. 3). Our data indicate that ZntB is a major endosomal ZnT [the signal is lower in phagosomes of *zntB* KO cells (Fig. 7A–C)], but membrane trafficking from other endosomes, such as recycling endosomes, or from the biosynthetic pathway (Golgi), which are positive for ZntC and ZntD, might contribute to endosomal  $\text{Zn}^{2+}$  levels. Unfortunately, it is not yet possible to measure precisely the contributions of each pathway and transporter to the  $\text{Zn}^{2+}$  concentration in the endosomal-phagosomal compartments. Nevertheless, we clearly document that zincosomes are of endosomal origin (lysosomal and postlysosomal, Fig. 1).

The seminal elemental analysis study of Wagner and colleagues revealed that the  $\text{Zn}^{2+}$  concentration inside the phagosomes containing various mycobacteria could reach high  $\mu\text{M}$  to mM levels (Wagner et al., 2005). Because the differential growth inhibition of wild type and the  $\Delta\text{zntA}$  *E. coli* mutant was observed at  $\text{Zn}^{2+}$  concentrations between 0.20 mM and 1.25 mM (Fig. 8B), we conclude that the concentration of  $\text{Zn}^{2+}$  inside the phagosome might be in the low mM range. Because of the limitations of the fluorescent probes available, an absolute quantitation of the  $\text{Zn}^{2+}$  concentration inside various organelles is likely not yet achievable.

It was suggested that the concentration of cytosolic  $\text{Zn}^{2+}$  fluctuates in response to various stimuli (Kambe et al., 2015). For instance, after incubation of macrophages with *E. coli*,  $\text{Zn}^{2+}$  is released from storage complexes, followed by pumping and sequestration into phagosomes. However, this was not observed in *Dictyostelium* by feeding cells with beads or with bacteria (Figs 2A,B and 8A; Fig. S5). We reason that, because the concentration of cytosolic  $\text{Zn}^{2+}$  is very low [between pM and low nM (Kambe et al., 2015)], it is consequently under the detection limit of FZ-3 and NBD-TPEA, explaining why we could not monitor cytosolic  $\text{Zn}^{2+}$ .

The subcellular homeostasis of  $\text{Zn}^{2+}$  is tightly regulated through uptake, storage, re-distribution and efflux mechanisms that are, among others, mediated by  $\text{Zn}^{2+}$  transporters of the ZnT and ZIP family (Bird, 2015). Seven members of the ZIP family and four members of the ZnT family have been identified in *Dictyostelium* (Dunn et al., 2018; Sunaga et al., 2008). ZntC and ZntD are the

*Dictyostelium* homologues of human ZNT6 (Huang et al., 2002) and ZNT7 (Kirschke and Huang, 2003), respectively. As their mammalian counterparts (Kambe et al., 2015), they localized at recycling endosomes and/or in the Golgi complex of *Dictyostelium* (Fig. 5A–G). ZntA, which is not closely related to any specific human  $\text{Zn}^{2+}$  transporter (Dunn et al., 2018), was located at the membrane of the CV (Figs 4A–C and 5G; Fig. S2A). *Dictyostelium* ZntB is the closest homologue of human ZNT1 (also known as SLC30A1) and ZNT10 (Dunn et al., 2018). Whereas Znt1 is a plasma membrane protein (Palmiter and Findley, 1995), Znt10 locates at the Golgi complex and at early and/or recycling endosomes (Patrushev et al., 2012), a location similar to the one of ZntB, described here (Fig. 4H). In addition, ZntB was observed at BCPs at the phagolysosomal stage (Fig. 4D–G; Fig. S3A,B). Loss of ZntB led to a 60% reduction of the FZ-3 fluorescence inside BCPs (Fig. 7A–E), leading to the conclusion that ZntB is the main endolysosomal  $\text{Zn}^{2+}$  transporter in *Dictyostelium* (Fig. 7F).

Interestingly, *Dictyostelium* growth was only inhibited by  $\text{Zn}^{2+}$  or  $\text{Cu}^{2+}$  concentrations at 50- or 500-fold the physiological levels, suggesting a very efficient control of  $\text{Zn}^{2+}$  and  $\text{Cu}^{2+}$  homeostasis (Buracco et al., 2018). In *Dictyostelium* cells, a classical metallothionein activity is not detected (Burlando et al., 2002), and consequently the CV was proposed to serve as a detoxification system for metal ions such as  $\text{Fe}^{2+}$ ,  $\text{Zn}^{2+}$  and  $\text{Cu}^{2+}$  (Bozzaro et al., 2013; Buracco et al., 2018; Peracino et al., 2013).

Changes in the cytosolic  $\text{Zn}^{2+}$  levels under non-steady-state conditions are remedied in a process described as ‘muffling’ by diverse mechanisms such as the cytosolic buffering by metallothioneins, the extrusion of  $\text{Zn}^{2+}$  from the cell and the sequestration of  $\text{Zn}^{2+}$  into organelles (Colvin et al., 2010). In *Dictyostelium*,  $\text{Zn}^{2+}$  is sequestered into the CV thanks to ZntA-mediated transport (Fig. 6A,B). We think that the increased  $\text{Zn}^{2+}$  levels found in lysosomes (Fig. 6D–G) and BCPs (Fig. 6H,I) of *zntA* KO cells indicate an unexpected crosstalk between the endosome-related water-pumping CV and the endosomal-phagosomal maturation pathway. Our data indicate that the CV plays a major role in regulating  $\text{Zn}^{2+}$  in *Dictyostelium*, and that incapacitating a CV  $\text{Zn}^{2+}$  transporter leads to a domino effect and increases the phagosomal-endosomal  $\text{Zn}^{2+}$  concentration, thereby leading to a more bactericidal environment (Fig. 8C).

Botella and colleagues revealed metal poisoning of ingested microbes as a novel killing strategy of macrophages (Botella et al., 2011). Besides  $\text{Zn}^{2+}$  poisoning, one can speculate that bacteria also have to face Cu poisoning inside the phagosome. In line with that hypothesis, NBD-TPEA was quenched at later phagocytic stages (Fig. 2A,C; Fig. S1C), a plausible sign of  $\text{Cu}^{2+}$  accumulation. Interestingly, the expression of the *Dictyostelium* homologue of the phagosomal Cu transporter ATP7A is upregulated upon feeding with bacteria, consistent with a possible role of Cu poisoning during phagocytosis (Hao et al., 2016; White et al., 2009).

Excess  $\text{Zn}^{2+}$  levels might inhibit bacterial ATP production by impairing the activity of cytochromes (Beard et al., 1995). Additionally, excess  $\text{Zn}^{2+}$  might replace other metals in the active site of various enzymes or occupy nonspecific binding sites (Nies, 1999). Here, we investigated the role of  $\text{Zn}^{2+}$  during phagocytosis and killing of bacteria by *Dictyostelium*.  $\text{Zn}^{2+}$  was observed inside phagosomes containing *E. coli* (Fig. 8A) and *M. smegmatis* (Fig. S5). Similar to the situation described in macrophages, an *E. coli* strain deficient in the  $\text{Zn}^{2+}$  efflux P<sub>1B</sub>-type ATPase ZntA was killed faster than the wild type (Fig. 8C,D), leading to the conclusion that  $\text{Zn}^{2+}$  poisoning belongs to the killing repertoire of *Dictyostelium*. Although the accumulation of  $\text{Zn}^{2+}$  inside lysosomes and BCPs of the *zntA* KO



led to a better killing capacity of *Dictyostelium* (Fig. 8C), bacteria killing in the *zntB* KO was unaffected (Fig. 8D). This suggests that  $Zn^{2+}$  poisoning is an evolutionarily conserved process and might act in concert with other killing factors, such as phagosomal acidification, reactive oxygen species production, and deprivation or poisoning by other metals, which would compensate for the loss of ZntB.

## MATERIALS AND METHODS

### *Dictyostelium* plasmids, strains and cell culture

All the *Dictyostelium* material used in the study is listed below (Table S1). *Dictyostelium* Ax2(Ka) and AX4 cells were cultured axenically at 22°C in HL5-C medium (Foremedium) supplemented with 100 U/ml penicillin and 100 µg/ml streptomycin to avoid contamination. Cell lines expressing fluorescent reporters and KO cell lines were cultured in the presence of selective antibiotics [hygromycin (50 µg/ml), neomycin (5 µg/ml) or blasticidin (5 µg/ml)]. To monitor the localization of ZnTs, *Dictyostelium* was transformed with plasmids carrying the ZntA-, ZntB-, ZntC- or ZntD-mCherry constructs [pDM1044 backbone (Veltman et al., 2009)]. The *zntA* KO was generated in the Ax2(Ka) background by homologous recombination following the one-step cloning protocol previously described (Wiegand et al., 2011). In brief, left and right arms of *zntA* were amplified using the primers 5'-AGCGCGTCTCCAATGCTGCAGGGAAGTGAGGGTGTG-3' (forward) and 5'-AGCGCGTCTCCGTTGGTTATGTTTCGTGTTTCATG-3' (reverse), and 5'-AGCGCGTCTCCCTTCCAACAATAGATCCCGAAG-3' (forward) and 5'-AGCGCGTCTCTCCCTGCAGGTGGATGTGCACTT-C-3' (reverse), and cloned into the StarGate® Acceptor Vector pKOS-IBA-Dicty1 using the StarGate cloning kit. The resulting plasmid was transformed into *Dictyostelium* by electroporation, and positive clones were selected with blasticidin (Fig. S4A). Correct integration into the genome was tested by PCR using different combinations of primers: *zntA* flanking forward 5'-CGATTGTGTTACCTAAATATTCGTG-3' and *zntA* flanking reverse 5'-CACCCAATTTACACTAGTTTCACC-3', *zntA* inside forward 5'-GTG-GTGAAGATGGTAGTAGTAGTG-3' and *zntA* inside reverse 5'-CATGA GTACACCTAAACTTTACAG-3', Bsr forward 5'-AGATCTTGTGAG-AAATGTTAAATTGATC-3' and Bsr reverse 5'-TTGAAGAACTCATT-CCACTCAATATAC-3' (Fig. S4B).

### Verification of the *zntB* REMI KO

The *zntB* KO (AX4 background) was obtained as part of the GWDI Project (<https://remi-seq.org>) and was generously provided by Prof. Christopher Thompson. The individual mutant was obtained from the grid. To confirm the insertion site of the blasticidin cassette into the *zntB* gene, genomic DNA was isolated from wild type and *zntB* KO using the High Pure PCR Template Preparation Kit (Roche), and diagnostic PCR was performed according to the recommendations on the GWDI website. Primer combinations with the two *zntB* specific primers, *zntB* forward 5'-GGCAATTCACGTTTCAT-CAG-3' and *zntB* reverse 5'-GTAACGAATTGAATCCAAATCG-3', binding ~400 bp up- or downstream the insertion sides, and the two primers specific for the blasticidin cassette pGWDI1, 5'-GTTGAGAAA-GTTTAAATTGATCC-3' and pGWDI2 5'-ATAGAAATGAATGGCAA-GTTAG-3', were used to confirm the insertion (Fig. S4C,D).

### *E. coli* and *M. smegmatis* strains and culture

*E. coli* wild type and  $\Delta zntA$  were kindly provided by Prof. Christopher Rensing (Rensing et al., 1997; Chinese Academy of Sciences Beijing, China), and cultured in LB medium. *M. smegmatis* (Hagedorn and Soldati, 2007) was cultured in 7H9 medium supplemented with 10% OADC, 0.05% Tween 80 and 0.2% glycerol at 32°C in shaking. Erlenmeyer flasks containing 5 mm glass beads were used to minimize clumping of bacteria. Vybrant DyeCycle Ruby Stain (Thermo Fisher Scientific) was used to stain intracellular *M. smegmatis* before live imaging was performed.

### Imaging of free $Zn^{2+}$ in *Dictyostelium*

The day before imaging, *Dictyostelium* was plated on two- or four-well ibidi dishes. Three hours before imaging, HL5-C was changed to SIH [Formedium, full synthetic medium with low  $Zn^{2+}$  concentration (2.3 mg/l  $ZnSO_4$ )]. After 2 h in SIH, cells were washed three times in Soerensen

buffer and stained with 2 µM FZ-3 (Thermo Fisher Scientific, F-24195; 400 µM stock in DMSO; Gee et al., 2002) or 5 µM NBD-TPEA (Sigma-Aldrich, N1040; 1 mM stock in DMSO; Qian et al., 2009) for 30 min in the dark. In order to synchronize phagocytosis, cells were cooled on a cold metal plate for 10 min before adding the 3 µm latex beads (Sigma-Aldrich, LB30). Beads were mixed with Soerensen buffer and added to the cells. After centrifugation at 500 g for 2 min at 4°C, the medium was carefully aspirated from the dish and an agarose overlay was placed on top of the cells, as described before (Barisch et al., 2015). Cells were imaged on an inverted 3i Marianas spinning disc confocal microscope using the 63× glycerol or 100× oil objectives. Where indicated, cells were treated for 3 h with different chelators: TPEN (Sigma-Aldrich, 87641), DTPA (Sigma-Aldrich, D6518) or  $CuSO_4 \cdot 5H_2O$  (Sigma-Aldrich, C3036) before and throughout staining with the  $Zn^{2+}$  probes. To label all endosomes, TRITC-dextran (70 kDa; Sigma-Aldrich, T1162); 1 mg/ml; stock 10 mg/ml in ddH<sub>2</sub>O) or Alexa Fluor 647-dextran (10 kDa; Molecular Probes, D22914; 30 µg/ml; 2 mg/ml stock in water) was added overnight and throughout FZ-3 and NBD-TPEA staining. To induce damage in lysosomes, cells were incubated with 7 mM LLome (Bachem, G-2550; 1 M stock in water). As a positive control for lysosomal damage, cells were treated with 0.2 mM of 524 Da HPTS (Molecular Probes, H348; 0.2 M stock in water).

To quantify the number of zincosomes inside wild type and *zntA* KO, cells were plated overnight on two-well ibidi slides. After staining with NBD-TPEA, images were taken using an ImageXpress spinning disc confocal microscope (Molecular Devices) and the number of zincosomes in wild type and *zntA* KO was assessed using MetaXpress (Molecular Devices).

The temporal and spatial dynamics of  $Zn^{2+}$  inside BCPs was quantified using ImageJ and the 'CenterOnClick' plugin (N. Roggli, University of Geneva, unpublished) that automatically centres the 'clicked' particle of interest in a recalculated image for further visualization and analysis. The integrated density inside a 'donut' that was drawn around the FZ-3 signal was measured using 'plot Z-axis profile'.

### Antibodies and immunofluorescence

Antibodies against p80 (Ravanel et al., 2001) were purchased from the Geneva antibody platform (University of Geneva, Switzerland). An anti-RFP antibody (Chromotek) was used to increase the fluorescence of mCherry-expressing fusion proteins. As secondary antibodies, goat anti-mouse, anti-rabbit and anti-rat IgG coupled to Alexa Fluor 488, Alexa Fluor 546 (Thermo Fisher Scientific) or CF640R (Biotium) were used. For immunofluorescence, *Dictyostelium* cells were fixed with cold MeOH or 4% paraformaldehyde, as described previously (Hagedorn et al., 2006). Images were recorded with a Zeiss LSM700 confocal microscope using a 63×/1.4 NA or a 100×/1.4 NA oil-immersion objective.

### In vitro effects of heavy metals on *E. coli* growth

*E. coli* wild type and  $\Delta zntA$  were grown in LB medium overnight at 37°C with shaking at 150 rpm. Bacteria were diluted to an optical density at a wavelength of 600 nm ( $OD_{600}$ ) of 0.1 and plated in 96-well plates containing LB medium with different concentrations of heavy metals (i.e.  $ZnSO_4$ ,  $CuSO_4$ ,  $FeCl_3$ ,  $MnCl_2$  from 0.05 mM to 2.5 mM). The  $OD_{600}$  was measured every hour using a 96-well plate reader (SpectraMax i3, Molecular Devices).

### Killing of bacteria and involvement of $Zn^{2+}$

Intracellular killing of *E. coli* wild type and  $\Delta zntA$  carrying a GFP-harboring plasmid (Valdivia and Falkow, 1997) was monitored as described previously (Leiba et al., 2017). A 1:10 dilution of overnight *E. coli* cultures was centrifuged for 4 min at 18,000 g and bacteria were resuspended in 300 µl filtered HL5-C. The bacterial suspension (10 µl) was plated on each well of a four-well ibidi slide and centrifuged for 10 min at 500 g. Then, 300 µl of a  $1 \times 10^6$  cells/ml *Dictyostelium* culture in LoFlo (synthetic low-fluorescent medium, Foremedium) was overlaid on the bacteria, and images were recorded at 22°C with a Leica AF6000 LX wide-field microscope using the 40× dry objective at 30 s intervals. For each phagocytosed bacterium, the time between phagocytosis and fluorescence extinction (killing) was determined manually using ImageJ, and the probability of bacterial survival was represented as a Kaplan-Meier

estimator. The data of three independent experiments were pooled and statistical comparisons between Kaplan–Meier curves were calculated using the log-rank test.

To monitor the involvement of  $Zn^{2+}$  in the killing of *E. coli*, *Dictyostelium* cells were stained with NBD-TPEA, as mentioned above, and bacteria were labelled using CF594 succinimidyl ester (SE) (Sigma-Aldrich, SCJ4600031). Briefly, an overnight culture of bacteria was diluted 1:10 in Soerensen buffer and incubated with 2  $\mu$ l of a 10 mM CF594 SE stock solution [in dimethyl sulfoxide (DMSO)] for 1 h in the dark. After two washes with Soerensen buffer, bacteria were resuspended in 1 ml filtered HL5-C. Subsequently, 10  $\mu$ l of the bacteria suspension was added to the pre-cooled cells on an eight-well ibidi slide and centrifuged onto cells for 1 min at 500 g at 4°C. Images were taken at 90 s intervals using a spinning disc confocal microscope with a 63 $\times$  objective.

#### Acknowledgements

We gratefully acknowledge the imaging platform of the University of Geneva for their expert and friendly support. We thank the GWDI Project (<https://remi-seq.org>) for the *zntB* REMI cell line. We are grateful to Prof. Michael Rensing for sharing the  $\Delta zntA$  *E. coli* KO. We thank Dr Elena Cardenal-Muñoz for careful reading and editing of the manuscript and thoughtful suggestions; Dr Olivier Schaad for helping with the statistics; Dr Monica Hagedorn and Prof. Markus Maniak for comments on the manuscript; and Dr Olivier Neyrolles for inspiring the project. T.S. is a member of IGE3 ([www.ige3.unige.ch](http://www.ige3.unige.ch)).

#### Competing interests

The authors declare no competing or financial interests.

#### Author contributions

Conceptualization: C.B., T.S.; Methodology: C.B., V.K., L.H.L., T.S.; Formal analysis: C.B., V.K., L.H.L., J.A., A.T.L.-J.; Investigation: C.B., V.K., L.H.L., J.A., A.T.L.-J.; Writing - original draft: C.B.; Writing - review & editing: C.B., L.H.L., T.S.; Visualization: C.B., V.K., J.A.; Supervision: C.B., T.S.; Project administration: T.S.; Funding acquisition: T.S.

#### Funding

This work was supported by Schweizerischer Nationalfonds zur Förderung der Wissenschaftlichen Forschung [310030\_149390].

#### Supplementary information

Supplementary information available online at <http://jcs.biologists.org/lookup/doi/10.1242/jcs.222000.supplemental>

#### References

- Barisch, C., Lopez-Jimenez, A. T. and Soldati, T. (2015). Live imaging of *Mycobacterium marinum* infection in *Dictyostelium discoideum*. In *Mycobacteria Protocols (Methods Mol Biol)*, vol. 1285 (ed. T. Parish and D. Roberts), pp. 369–385. Humana, NYC.
- Beard, S. J., Hughes, M. N. and Poole, R. K. (1995). Inhibition of the cytochrome bd-terminated NADH oxidase system in *Escherichia coli* K-12 by divalent metal cations. *FEMS Microbiol. Lett.* **131**, 205–210.
- Benghezal, M., Gotthardt, D., Cornillon, S. and Cosson, P. (2001). Localization of the Rh50-like protein to the contractile vacuole in *Dictyostelium*. *Immunogenetics* **52**, 284–288.
- Bird, A. J. (2015). Cellular sensing and transport of metal ions: implications in micronutrient homeostasis. *J. Nutr. Biochem.* **26**, 1103–1115.
- Bosomworth, H. J., Thornton, J. K., Coneyworth, L. J., Ford, D. and Valentine, R. A. (2012). Efflux function, tissue-specific expression and intracellular trafficking of the  $Zn^{2+}$  transporter ZnT10 indicate roles in adult  $Zn^{2+}$  homeostasis. *Metallomics* **4**, 771–779.
- Botella, H., Peyron, P., Levillain, F., Poincloux, R., Poquet, Y., Brandli, I., Wang, C., Tailleux, L., Tilleul, S., Charriere, G. M. et al. (2011). Mycobacterial p(1)-type ATPases mediate resistance to zinc poisoning in human macrophages. *Cell Host Microbe* **10**, 248–259.
- Bozzaro, S., Bucci, C. and Steinert, M. (2008). Phagocytosis and host-pathogen interactions in *Dictyostelium* with a look at macrophages. *Int. Rev. Cell Mol. Biol.* **271**, 253–300.
- Bozzaro, S., Buracco, S. and Peracino, B. (2013). Iron metabolism and resistance to infection by invasive bacteria in the social amoeba *Dictyostelium discoideum*. *Front. Cell Infect. Microbiol.* **3**, 50.
- Bracco, E., Peracino, B., Noegel, A. A. and Bozzaro, S. (1997). Cloning and transcriptional regulation of the gene encoding the vacuolar/H<sup>+</sup> ATPase B subunit of *Dictyostelium discoideum*. *FEBS Lett.* **419**, 37–40.
- Buckley, C. M., Heath, V. L., Gueho, A., Bosmani, C., Knobloch, P., Sikakana, P., Personnic, N., Dove, S. K., Michell, R. H., Meier, R. et al. (2018). PIKfyve/Fab1 is required for efficient V-ATPase and hydrolase delivery to phagosomes, phagosomal killing, and restriction of *Legionella* infection. *bioRxiv* **343301**.
- Buracco, S., Peracino, B., Andreini, C., Bracco, E. and Bozzaro, S. (2018). Differential Effects of Iron, Zinc, and Copper on *Dictyostelium discoideum* Cell Growth and Resistance to *Legionella pneumophila*. *Front. Cell Infect. Microbiol.* **7**, 536.
- Burlando, B., Evangelisti, V., Dondero, F., Pons, G., Camakaris, J. and Viarengo, A. (2002). Occurrence of Cu-ATPase in *Dictyostelium*: possible role in resistance to copper. *Biochem. Biophys. Res. Commun.* **291**, 476–483.
- Carnell, M., Zech, T., Calaminus, S. D., Ura, S., Hagedorn, M., Johnston, S. A., May, R. C., Soldati, T., Machesky, L. M. and Insall, R. H. (2011). Actin polymerization driven by WASH causes V-ATPase retrieval and vesicle neutralization before exocytosis. *J. Cell Biol.* **193**, 831–839.
- Chan, H., Babayan, V., Blyumin, E., Gandhi, C., Hak, K., Harake, D., Kumar, K., Lee, P., Li, T. T., Liu, H. Y. et al. (2010). The p-type ATPase superfamily. *J. Mol. Microbiol. Biotechnol.* **19**, 5–104.
- Charette, S. J., Mercanti, V., Letourneur, F., Bennett, N. and Cosson, P. (2006). A role for adaptor protein-3 complex in the organization of the endocytic pathway in *Dictyostelium*. *Traffic* **7**, 1528–1538.
- Colvin, R. A., Holmes, W. R., Fontaine, C. P. and Maret, W. (2010). Cytosolic zinc buffering and muffling: their role in intracellular zinc homeostasis. *Metallomics* **2**, 306–317.
- Djoko, K. Y., Ong, C.-L., Walker, M. J. and McEwan, A. G. (2015). The role of copper and zinc toxicity in innate immune defense against bacterial pathogens. *J. Biol. Chem.* **290**, 18954–18961.
- Ducret, V., Gonzalez, M. R., Scignari, T. and Perron, K. (2016). OprD Repression upon metal treatment requires the RNA chaperone Hfq in *Pseudomonas aeruginosa*. *Genes (Basel)* **7**, E82.
- Dunn, J. D., Bosmani, C., Barisch, C., Raykov, L., Lefrançois, L. H., Cardenal-Munoz, E., Lopez-Jimenez, A. T. and Soldati, T. (2018). Eat prey, live: *dictyostelium discoideum* as a model for cell-autonomous defenses. *Front. Immunol.* **8**, 1906.
- Flannagan, R. S., Heit, B. and Heinrichs, D. E. (2015). Antimicrobial mechanisms of macrophages and the immune evasion strategies of *Staphylococcus aureus*. *Pathogens* **4**, 826–868.
- Gee, K. R., Zhou, Z.-L., Qian, W.-J. and Kennedy, R. (2002). Detection and imaging of zinc secretion from pancreatic beta-cells using a new fluorescent zinc indicator. *J. Am. Chem. Soc.* **124**, 776–778.
- Gonzalez, M. R., Ducret, V., Leoni, S. and Perron, K. (2018). *Pseudomonas aeruginosa* zinc homeostasis: Key issues for an opportunistic pathogen. *Biochim. Biophys. Acta* **S1874-9399(17)30297-3**.
- Gotthardt, D., Warnatz, H. J., Henschel, O., Brückert, F., Schleicher, M. and Soldati, T. (2002). High-resolution dissection of phagosome maturation reveals distinct membrane trafficking phases. *Mol. Biol. Cell* **13**, 3508–3520.
- Hacker, U., Albrecht, R. and Maniak, M. (1997). Fluid-phase uptake by macropinocytosis in *Dictyostelium*. *J. Cell Sci.* **110**, 105–112.
- Hagedorn, M. and Soldati, T. (2007). Flotillin and RacH modulate the intracellular immunity of *Dictyostelium* to *Mycobacterium marinum* infection. *Cell. Microbiol.* **9**, 2716–2733.
- Hagedorn, M., Neuhaus, E. M. and Soldati, T. (2006). Optimized fixation and immunofluorescence staining methods for *Dictyostelium* cells. *Methods Mol. Biol.* **346**, 327–338.
- Hao, X., Lüthje, F., Ronn, R., German, N. A., Li, X., Huang, F., Kisaka, J., Huffman, D., Alwathnani, H. A., Zhu, Y. G. et al. (2016). A role for copper in protozoan grazing - two billion years selecting for bacterial copper resistance. *Mol. Microbiol.* **102**, 628–641.
- Heuser, J., Zhu, Q. and Clarke, M. (1993). Proton pumps populate the contractile vacuoles of *Dictyostelium amoebae*. *J. Cell Biol.* **121**, 1311–1327.
- Huang, L., Kirschke, C. P. and Gitschier, J. (2002). Functional characterization of a novel mammalian zinc transporter, ZnT6. *J. Biol. Chem.* **277**, 26389–26395.
- Kambe, T., Tsuji, T., Hashimoto, A. and Itsumura, N. (2015). The physiological, biochemical, and molecular roles of zinc transporters in zinc homeostasis and metabolism. *Physiol. Rev.* **95**, 749–784.
- Kapetanovic, R., Bokil, N. J., Achard, M. E., Ong, C. Y., Peters, K. M., Stocks, C. J., Phan, M. D., Monteleone, M., Schroder, K., Irvine, K. M. et al. (2016). *Salmonella* employs multiple mechanisms to subvert the TLR-inducible zinc-mediated antimicrobial response of human macrophages. *FASEB J.* **30**, 1901–1912.
- Kehl-Fie, T. E. and Skaar, E. P. (2010). Nutritional immunity beyond iron: a role for manganese and zinc. *Curr. Opin. Chem. Biol.* **14**, 218–224.
- Kirschke, C. P. and Huang, L. (2003). ZnT7, a novel mammalian zinc transporter, accumulates zinc in the Golgi apparatus. *J. Biol. Chem.* **278**, 4096–4102.
- Kirsten, J. H., Xiong, Y., Davis, C. T. and Singleton, C. K. (2008). Subcellular localization of ammonium transporters in *Dictyostelium discoideum*. *BMC Cell Biol.* **9**, 71.
- Kolaj-Robin, O., Russell, D., Hayes, K. A., Pembroke, J. T. and Soulimane, T. (2015). Cation diffusion facilitator family: structure and function. *FEBS Lett.* **589**, 1283–1295.



- Leiba, J., Sabra, A., Bodinier, R., Marchetti, A., Lima, W. C., Melotti, A., Perrin, J., Burdet, F., Pagni, M., Soldati, T. et al. (2017). Vps13F links bacterial recognition and intracellular killing in Dictyostelium. *Cell. Microbiol.* **19**, e12722.
- Lopez, C. A. and Skaar, E. P. (2018). The impact of dietary transition metals on host-bacterial interactions. *Cell Host Microbe* **23**, 737-748.
- Lopez-Jimenez, A. T., Cardenal Munoz, E., Leuba, F., Gerstenmaier, L., Hagedorn, M., King, J. S. and Soldati, T. (2018). ESCRT and autophagy cooperate to repair ESX-1-dependent damage to the Mycobacterium-containing vacuole. *bioRxiv* **334755**.
- Marchetti, A., Lelong, E. and Cosson, P. (2009). A measure of endosomal pH by flow cytometry in Dictyostelium. *BMC Res Notes* **2**, 7.
- McDevitt, C. A., Ogunniyi, A. D., Valkov, E., Lawrence, M. C., Kobe, B., McEwan, A. G. and Paton, J. C. (2011). A molecular mechanism for bacterial susceptibility to zinc. *PLoS Pathog.* **7**, e1002357.
- Neuhaus, E. M., Horstmann, H., Almers, W., Maniak, M. and Soldati, T. (1998). Ethane-freezing/methanol-fixation of cell monolayers: a procedure for improved preservation of structure and antigenicity for light and electron microscopies. *J. Struct. Biol.* **121**, 326-342.
- Neuhaus, E. M., Almers, W. and Soldati, T. (2002). Morphology and dynamics of the endocytic pathway in Dictyostelium discoideum. *Mol. Biol. Cell* **13**, 1390-1407.
- Nies, D. H. (1999). Microbial heavy-metal resistance. *Appl. Microbiol. Biotechnol.* **51**, 730-750.
- Ong, C.-L., Gillen, C. M., Barnett, T. C., Walker, M. J. and McEwan, A. G. (2014). An antimicrobial role for zinc in innate immune defense against group A streptococcus. *J. Infect. Dis.* **209**, 1500-1508.
- Palmiter, R. D. and Findley, S. D. (1995). Cloning and functional characterization of a mammalian zinc transporter that confers resistance to zinc. *EMBO J.* **14**, 639-649.
- Patrushev, N., Seidel-Rogol, B. and Salazar, G. (2012). Angiotensin II requires zinc and downregulation of the zinc transporters ZnT3 and ZnT10 to induce senescence of vascular smooth muscle cells. *PLoS ONE* **7**, e33211.
- Peracino, B., Wagner, C., Balest, A., Balbo, A., Pergolizzi, B., Noegel, A. A., Steinert, M. and Bozzaro, S. (2006). Function and mechanism of action of Dictyostelium Nramp1 (Slc11a1) in bacterial infection. *Traffic* **7**, 22-38.
- Peracino, B., Buracco, S. and Bozzaro, S. (2013). The Nramp (Slc11) proteins regulate development, resistance to pathogenic bacteria and iron homeostasis in Dictyostelium discoideum. *J. Cell Sci.* **126**, 301-311.
- Pyle, C. J., Azad, A. K., Papp, A. C., Sadee, W., Knoell, D. L. and Schlesinger, L. S. (2017). Elemental ingredients in the macrophage cocktail: role of zip8 in host response to Mycobacterium tuberculosis. *Int. J. Mol. Sci.* **18**.
- Qian, F., Zhang, C., Zhang, Y., He, W., Gao, X., Hu, P. and Guo, Z. (2009). Visible light excitable Zn<sup>2+</sup> fluorescent sensor derived from an intramolecular charge transfer fluorophore and its in vitro and in vivo application. *J. Am. Chem. Soc.* **131**, 1460-1468.
- Ravanel, K., de Chasse, B., Cornillon, S., Benghezal, M., Zulianello, L., Gebbie, L., Letourneur, F. and Cosson, P. (2001). Membrane sorting in the endocytic and phagocytic pathway of Dictyostelium discoideum. *Eur. J. Cell Biol.* **80**, 754-764.
- Rensing, C., Mitra, B. and Rosen, B. P. (1997). The zntA gene of Escherichia coli encodes a Zn(II)-translocating P-type ATPase. *Proc. Natl. Acad. Sci. USA* **94**, 14326-14331.
- Repnik, U., Borg Distefano, M., Speth, M. T., Ng, M. Y. W., Progida, C., Hoflack, B., Gruenberg, J. and Griffiths, G. (2017). L-leucyl-L-leucine methyl ester does not release cysteine cathepsins to the cytosol but inactivates them in transiently permeabilized lysosomes. *J. Cell Sci.* **130**, 3124-3140.
- Sattler, N., Monroy, R. and Soldati, T. (2013). Quantitative analysis of phagocytosis and phagosome maturation. *Methods Mol. Biol.* **983**, 383-402.
- Soldati, T. and Neyrolles, O. (2012). Mycobacteria and the intraphagosomal environment: take it with a pinch of salt(s)! *Traffic* **13**, 1042-1052.
- Subramanian Vignesh, K., Landero Figueroa, J. A., Porollo, A., Caruso, J. A. and Deepe, G. S. Jr. (2013). Granulocyte macrophage-colony stimulating factor induced Zn sequestration enhances macrophage superoxide and limits intracellular pathogen survival. *Immunity* **39**, 697-710.
- Sunaga, N., Monna, M., Shimada, N., Tsukamoto, M. and Kawata, T. (2008). Expression of zinc transporter family genes in Dictyostelium. *Int. J. Dev. Biol.* **52**, 377-381.
- Uchikawa, T., Yamamoto, A. and Inouye, K. (2011). Origin and function of the stalk-cell vacuole in Dictyostelium. *Dev. Biol.* **352**, 48-57.
- Valdivia, R. H. and Falkow, S. (1997). Probing bacterial gene expression within host cells. *Trends Microbiol.* **5**, 360-363.
- Veltman, D. M., Akar, G., Bosgraaf, L. and Van Haastert, P. J. M. (2009). A new set of small, extrachromosomal expression vectors for Dictyostelium discoideum. *Plasmid* **61**, 110-118.
- Vinkenborg, J. L., Nicolson, T. J., Bellomo, E. A., Koay, M. S., Rutter, G. A. and Merx, M. (2009). Genetically encoded FRET sensors to monitor intracellular Zn<sup>2+</sup> homeostasis. *Nat. Methods* **6**, 737-740.
- Wagner, D., Maser, J., Lai, B., Cai, Z., Barry, C. E., III, Honer Zu Bentrop, K., Russell, D. G. and Bermudez, L. E. (2005). Elemental analysis of Mycobacterium avium-, Mycobacterium tuberculosis-, and Mycobacterium smegmatis-containing phagosomes indicates pathogen-induced microenvironments within the host cell's endosomal system. *J. Immunol.* **174**, 1491-1500.
- Weiss, G. and Carver, P. L. (2018). Role of divalent metals in infectious disease susceptibility and outcome. *Clin. Microbiol. Infect.* **24**, 16-23.
- White, C., Lee, J., Kambe, T., Fritzsche, K. and Petris, M. J. (2009). A role for the ATP7A copper-transporting ATPase in macrophage bactericidal activity. *J. Biol. Chem.* **284**, 33949-33956.
- Wiegand, S., Kruse, J., Gronemann, S. and Hammann, C. (2011). Efficient generation of gene knockout plasmids for Dictyostelium discoideum using one-step cloning. *Genomics* **97**, 321-325.
- Wienke, D., Drengk, A., Schmauch, C., Jenne, N. and Maniak, M. (2006). Vacuolin, a flotillin/reggie-related protein from Dictyostelium oligomerizes for endosome association. *Eur. J. Cell Biol.* **85**, 991-1000.
- Xu, Z., Gunn-Hee, K., Su, J. H., Min, J. J., Chongmok, L., Injae, S. and Yoon, J. (2009). An NBD-based colorimetric and fluorescent chemosensor for Zn<sup>2+</sup> and its use for detection of intracellular zinc ions. *Tetrahedron* **65**, 2307-2312.
- Yates, R. M., Hermetter, A. and Russell, D. G. (2005). The kinetics of phagosome maturation as a function of phagosome/lysosome fusion and acquisition of hydrolytic activity. *Traffic* **6**, 413-420.